

Numerical and experimental analysis for solidification and residual stress in the GMAW process for AISI 304 stainless steel

J. CHOI*, J. MAZUMDER

Center for Laser-Aided Intelligent Manufacturing, Department of Mechanical Engineering, University of Michigan at Ann Arbor, Ann Arbor, MI 48109, USA
E-mail: mazumder@umich.edu

Gas Metal Arc Welding (GMAW) process was analyzed by combining a finite element thermomechanical model for temperature and stress with solidification model. Model prediction was compared with experimental data in order to validate the model. The effects of welding process parameters on these welding fields were analyzed and reported. The effort to correlate the residual stress and solidification was initiated, yielding some valuable results. The solidification process was simulated using the formulation based on the Hunt-Trivedi model. Based on the temperature history, solidification speed and primary dendrite arm spacing were predicted at given nodes of interest. Results show that the variation during solidification is usually within an order of magnitude. The temperature gradient was generally in the range of 10^4 – 10^5 K/m for the given welding conditions (welding power = 6 kW and welding speed = 3.39 to 7.62 mm/sec), while solidification speed appeared to slow down from an order of 10^{-2} to 10^{-3} m/sec during solidification. SEM images revealed that the Primary Dendrite Arm Spacing (PDAS) fell in the range of 10^1 – 10^2 μm . The range of predicted sizes was in agreement with the experimental values. It was observed that the average size of the PDAS was dependent upon the welding speed. The PDAS fell between 7.5 to 20 μm for columnar and 10 to 30 μm for equiaxed dendrites, for welding speeds between 3.39 to 7.62 mm/sec. When the welding speed increased, it was observed that the average size of the PDAS decreased, as the model had predicted. For grain growth at the Heat Affected Zone (HAZ), Ashby's model was employed, and the prediction was in agreement with experimental results. For the residual stress calculation, the same mesh generation used in the heat transfer analysis was applied to make the simulation consistent. The analysis consisted of a transient heat analysis followed by a thermal stress analysis. An experimentally measured strain history was compared with the simulated result. The relationship between microstructure and the stress/strain field of welding was also obtained. © 2002 Kluwer Academic Publishers

1. Introduction

Welding is a complex process that involves many dependent variables which control the final microstructures and, consequently, mechanical properties of the weldment. Gas-metal-arc welding (GMAW) is usually a semiautomatic or automatic process in which an arc is struck between the filler metal and the workpiece, thus, supplying heat. This process inherently includes many nonlinear phenomena due to non-uniform heat flow and requires detailed analysis informed by rigorous scientific understanding in order to control and produce defect-free weldments. Heat transfer, solidification, and stress analysis in the weldment are necessary for a complete understanding of this process in order to offer the theoretical background to prevent

experimental trial-and-error. With the appearance of new computer hardware and software, mathematical modeling simulating such a sophisticated problem is now possible.

New developments in computer programs and the availability of high-speed digital computers have been combined to provide a better understanding of the residual stresses due to welding and to identify and evaluate means for controlling weld residual stresses. Analysis capabilities have expanded from analytical methods to more sophisticated, nonlinear, finite element based analysis techniques. Both the temperature analysis and elastic-plastic thermal stress analysis portions of residual stress models have been conducted with finite element analysis.

* Present Address: University of Missouri at Rolla, USA.

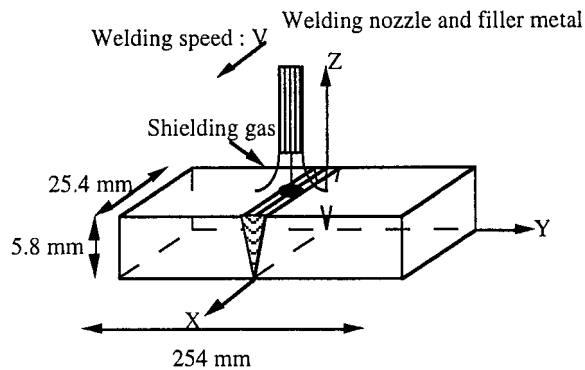


Figure 1 Schematic diagram for three dimensional GMAW process.

The GMAW process uses the filler metal as a consumable electrode through the center of the weld nozzle, as shown in Fig. 1. In this case, when the electrode comes close to the workpiece, an arc is struck between the filler metal and the workpiece, and the filler metal melts and joins two plates by filling a V-groove between the two plates. Shielding gas, a mixture of argon and oxygen gas, which flows through the annulus around the nozzle, is simultaneously employed with the filler metal in order to protect the weld from atmospheric contamination. The model is incorporated the following assumptions: (1) A part of the heat supplied by the arc is consumed to melt the wire electrode continuously. (2) A part of the heat is lost to the surroundings before the plates receive it. (3) The arc beam power distribution is considered to be Gaussian. (4) The heat of the arc and the molten metal joining the workpiece induces heat flow in all three dimensions of the workpiece. (5) Heat is lost from the surface in the form of convection and radiation. (6) The flow of the shielding gas causes enhanced convective heat loss from a part of the surface. The weld data used in this analysis are summarized in Table I.

TABLE I Welding data

Item	Data
Welding Voltage (V)	30.3 V
Welding current (I)	200 A
Arc efficiency (η)	0.67
Welding speed (v)	3.387 mm/sec 5.08 mm/sec 7.62 mm/sec
Arc beam radius (r_b)	5.56 mm
Filler wire diameter	1.6 mm
Filler wire feedrate	55.5 mm/sec
Nozzle diameter (D)	19.05 mm
Nozzle-to-plate distance (NPD)	19.05 mm
Nozzle angle with vertical (α)	0°
Ambient temperature (T_a)	294 K
Filler droplet temperature	2300 K
Solidus temperature (T_S)	1703 K
Liquidus temperature (T_L)	1730 K
Latent heat of fusion (L)	273790 J/kg
Density (ρ)	7887 kg/m ³
Shielding gas (98% Ar + 2%O ₂)	
Flow rate	0.24 Liter/sec (30 ft ³ /hr)
Thermal conductivity (k_{gas})	0.0178 W/m/K
Specific heat ($C_{p, gas}$)	518.82 J/kg/K
Dynamic viscosity (μ_{gas})	2.22×10^{-5} kg/m/sec
Density (ρ_{gas})	1.78 kg/m ³

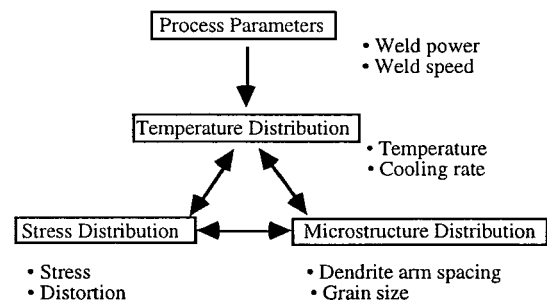


Figure 2 Interrelationship of weld controlling fields with process parameters.

The aim of this research is to develop a three-dimensional transient mathematical model that connects heat transfer history via solidification history to stress history. If achieved and verified, one can correlate microstructure history to residual stress history—something that has not been done in theoretical or mathematical form. The relationship between microstructure and residual stress could offer useful information for evaluating crack initiation and propagation during the GMAW process. In addition to it, the relationship between microstructures and weld process parameters can be predicted so that one can get a well-controlled weld microstructure under given process parameters.

The temperature history is the necessary input for the prediction of the time-dependent solidification and mechanical behaviors of the weldment. For a given design requirement to meet quality standards, the model might be useful in optimizing the process parameters since it could give the history information of temperatures and solidification microstructure parameters as well as residual stresses.

The interrelationship of weld controlling fields (temperature, microstructure, and stress field) with process parameters can be seen in Fig. 2. For a given processing parameter, first, temperature distribution, secondly, microstructure distribution, and finally, residual stress distribution will be predicted. Then the residual stress will be correlated with the microstructure and characterized. To both the welder and welding engineer, this information will be beneficial in helping to solve practical difficulties.

In order to achieve the goal, two approaches—numerical and experimental—were adapted. For the numerical approach, a 3-D transient finite element model was adapted. This includes: heat transfer analysis, which is a conduction model with convective and radiative boundary conditions; stress analysis, which will be used with a rate-independent plastic model with kinematic hardening and the Von Mises yield criteria. Microstructure analysis was equipped with the Hunt-Trivedi model, with the steady state growth condition in the fusion zone, and Ashby's diffusion-controlled grain growth model at the HAZ.

There have been many efforts to model the welding process. Rosenthal [1, 2] was the first to introduce the analytical solutions for the moving point and line heat source problem in welding and, later, Myers *et al.* [3] summarized these analytical works and stated the

TABLE II Modeling of weld pool convection (FDM)

Year	Author	Model	Problem and Driving force
1980	Athey [4]	2-D, steady	axisym, S arc, MHD ^a
1984	Oreper and Szekely [5]	2-D, transient	axisym, S arc, MHD, B, ST
1984	Chan, Mazumder and Chen [6]	2-D, transient	axisym, M laser, ST
1985	Kou and Sun [7]	2-D, steady	axisym, S arc, MHD, B, ST
1986	Kou and Wang [8, 9]	3-D, steady	M, laser, B, ST
1987	Chan, Mazumder and Chen [10, 11]	3-D, transient	axisym, M laser, B, ST
1989	Zacharia, Eraslan, Aldun and David [12]	3-D, transient	M arc, MHD, B, ST
1990	Zehr, Mazumder and Chen [13]	3-D, steady	M laser, B, ST
1993	Ducharme, Williams, and Kapadia [14]	3-D, transient	key hole, M Laser, B, ST

^aMHD = Magneto-Hydro-Dynamic, ST = Surface Tension, B = Buoyancy, S = Stationary, M = Moving.

TABLE III Modeling of welding (FEM)

Year	Author	Model	Analysis
1973	Hibbitt and Marcal [15]	2-D, steady	axisym, GMAW, heat transfer and stress
1975	Friedman [16]	2-D, plane stress	axisym, S arc, heat transfer and stress
1978	Andersson [17]	2-D, steady	axisym, SABW ^a , heat transfer and stress
1980	Rybicki [18]	2-D, quasi-steady	axisym, multi-pass girth butt weld, heat transfer and stress
1981	Andersson and Karlsson [19]	2-D, plane stress	butt weld, heat transfer and stress, crack
1982	Argysis [20]	3-D, transient	axisym, S arc, thermo-elastic and visco-plastic
1983	Stitt and Mazumder [21]	3-D, transient	axisym, GTAW, heat transfer
1986	Goldak <i>et al.</i> [22]	3-D, transient	M arc, thermo-elasto-plastic combined isotropic-kinematic hardening
1988	Mahin <i>et al.</i> [23]	2-D, plane stress	PASTA ^b , GTAW, thermal and stress
1989	Pardo and Weckman [24]	3-D, steady	axisym, GMAW, heat transfer
1989	Tekriwal and Mazumder [25]	3-D, transient	ABAQUS ^c , multi-pass GTAW and GMAW, heat transfer and stress, kinematic hardening

^aSABW = Submerged Arc Butt Welding.

^bPASTA = Program for Applications to Stress and Thermal Analysis (Sandia NL).

^cABAQUS = Commercial code by Hibbitt, Karlsson and Sorenson, Inc.

simplifying assumptions which limit the use of these models. There are several fields which have recently drawn much attention; such as weld pool convection modeling [4–11, 26], modeling of the arc or weld torch [21, 27], heat affected zone modeling with phase change [28–30], fusion zone dendrite and/or cell transition modeling, and weld residual stress modeling with thermal history, etc. Table II summarizes the modeling of weld pool convection using finite difference method (FDM). However, in the case of GMAW, only a few droplets are added at a time to the molten pool, thus the weld-pool-convection phenomena are short and may be neglected in comparison to the overall heat flow in the process.

Hibbitt and Marcall's paper [15] was the first to simulate the GMAW process. Using the finite element method (FEM), the thermal model was developed by uncoupling the mechanical aspect of the problem. Since then, as shown in Table III, many researchers have reported weld models to simulate thermal and stress fields during the welding process. Kraus [31] has developed an optical spectral radiometric/laser reflectance experimental method to measure the surface temperature on gas-tungsten-arc (GTA) welds in order to verify mathematical models.

However, there is also a great need for predicting the microstructure evolution during welding. Earlier works have not taken the solidification microstructure evolution into account and, therefore, complete explana-

TABLE IV History of solidification microstructures developments

Year	Author	Model/Theory
1935	Papapetrou [32]	Dendrite growth model (paraboloid)
1947	Ivantsov [33]	Isotherm dendrite theory (exact solution, paraboloid)
1963	Mullins and Sekerka [34, 35]	Instability growth theory
1964	Voronkov [36]	Instability growth theory
1966	Jackson and Hunt [37]	Eutectic growth theory
1973	Oldfield [38]	Computational growth model (non-steady state, perturbation)
1978	Langer and Müller-Krumbhaar [39]	Marginal stability theory Dynamic growth theory (LMK model)
1979	Hunt [40]	Cellular-dendrite theory (Marginal stability theory)
1981	Kurz and Fisher [41]	Cellular-dendrite theory (Kurz-Fisher model)
1984	Trivedi [42]	Dendrite growth model (Hunt-Trivedi model)
1991	Magnin and Trivedi [43]	Eutectic growth theory (modified Jackson-Hunt theory)

tions of the GMAW process have not been achieved yet. Table IV lists the brief history of solidification microstructure developments.

There have been many efforts to simulate solidification processing using mathematical models in order to analyze the welding process [44–47]. The difficulties

in modeling solidification usually come from the difficulty in incorporating the microscopic aspects of the model with the macroscopic aspects of the process. As Rappaz [48] pointed out, this field is still in the early stage of development, and most of the basic concepts have not been systematically implemented into solidification modeling codes, although they have already been outlined.

Micro-macroscopic modeling has already been attempted and has answered some of these questions. Primary phase formation in hypoeutectic alloys [49, 50] and grain size and secondary arm spacing [51] were predicted by some researchers. However, the prediction of microstructural features and comparison with experimental data are not yet reported in most papers on micro-macroscopic modeling. Giamei [52] reported that the barriers to solidification process modeling are being overcome because the rapid advancements in computer hardware and software have accelerated the implementation of solidification process modeling. The solidification and solid-state transformations that occur during the high-energy density welding of austenitic stainless steel, were also studied by Brooks *et al.* [53].

Ashby and Easterling contributed the first report on diagrams for grain growth in welds in 1982 [28]. In 1984, Ion *et al.* [29] developed a second report on diagrams of microstructure and hardness for heat-affected zones in welds. In predicting microstructure and hardenability in low alloy steels, Kirkaldy and Venugopalan [30] proposed volume fraction formulas for low alloy steels and constructed the predicted IT (Isothermal-Transformation) curve and the CCT (Continuous-Cooling-Transformation) curve. Recently, Watt *et al.* [54] proposed an algorithm for forecasting the microstructural development in weld HAZ with the computer algorithm originally developed for predicting the hardenability of low alloy steels by Kirkaldy [30].

2. Mathematical modeling

It is critical to decide the proper method of analysis in order to accommodate as many welding variables as possible and accurately predict the transient temperature distribution. The temperature history plays an important role in determining the size of the fusion and heat affected zones as well as grain size and growth pattern, and, consequently, residual stress distribution and distortion. Temperature-dependent material data was used as inputs for these modeling and process conditions, which were modified through reasonable assumptions based on engineering and economic points of view.

2.1. Process conditions

For heat transfer analysis:

- Arc heat flux (Gaussian distribution)

$$q(x, y, z, t) = -(\nabla KT) \quad (1)$$

- Convective boundary condition enhanced due to shielding gas

$$-(\nabla KT) = h(T - T_\infty) \quad (2)$$

- Symmetry plane ($y = 0$ plane)

$$(\nabla KT) = 0 \quad \text{at } y = 0 \quad \text{plane} \quad (3)$$

- Convective boundary condition

$$-(\nabla KT) = h(T - T_\infty) \quad (4)$$

- Radiation boundary condition

$$-(\nabla KT) = \varepsilon\sigma(T^4 - T_\infty^4) \quad (5)$$

For stress analysis:

In tensor form, the equations of force equilibrium would be written

$$\frac{\partial S_{ij}}{\partial x_{ij}} + \rho f_j = 0 \quad (6)$$

where ρ is the density and f_j is body forces per unit mass acting in the direction j . The moment or couple equilibrium conditions lead to that stress tensor is symmetric in the absence of any coupled body forces.

$$S_{ij} = S_{ji} \quad (7)$$

In the displacement formulation, the essential boundary conditions were $u = 0$ for the clamped portion of the plate surface and the normal displacement, u_y , equals 0 for the plane of symmetry at the $y = 0$ plane. Natural boundary conditions were embedded in the finite element formulation and were given as zero traction on the free surface of the plate. ($S_{ii} = 0$)

As in the usual classical plasticity, the following strain rate decomposition was used,

$$d\dot{\varepsilon}_{ij}^{tot} = d\dot{\varepsilon}_{ij}^{el} + d\dot{\varepsilon}_{ij}^{pl} + d\dot{\varepsilon}_{ij}^{th} \quad (8)$$

Creep strain was neglected, as in most welding analysis, based on the fact that high temperatures exist only for a very short period during welding. When a material at high temperature ($>0.3 T_{MP}$) is subjected to a continuous force (quasi-static condition), or to a force for a considerable time, the creep strain must be considered. Phase transformation strain was not included, since the finite element code in this analysis does not support it, and may result in small errors in the final analysis.

The effect of the strain rate is very small, because of the welding process characteristics. Usually, its rate is much faster than that of the casting process (and the creep effect is also negligible). Generally, thermo-mechanical properties under a high strain rate, for instance, 10^{-2} – 10^{-3} , are chosen. The kinematic hardening rule, which was proposed by Prager [55] and modified by Ziegler [56], was applied for the thermal load, which might exceed the yield stress locus.

For solidification analysis:

The H-T (Hunt-Trivedi) model for dendrite growth [40, 42] was adapted. The steady state condition was assumed in this model. Using the mass balance condition, the continuity of matter equation must be satisfied everywhere on the solid-liquid interface

$$V_n(C_I^L - C_I^S) + D \frac{\partial C}{\partial n} = 0 \quad (9)$$

where V_n is the velocity normal to the interface, the subscript I refers to the interface, the superscript L and S to liquid and solid, and $\partial C/\partial \tilde{n}$ is the concentration gradient normal to the interface. Assuming that the region close to the tip can be approximated as a part of the sphere, Hunt derived the following relationship between the primary spacing, λ , and the tip radius, R

$$\frac{G\lambda^2}{R} = -4\sqrt{2} \left[mC_i(1-k) + \frac{GD}{V} \right]. \quad (10)$$

For dendritic growth analysis, the Hunt model can be simplified since the first term on the right side of the above equation is dominant, and the value of R is given by the dendrite tip stability criterion of Trivedi

$$R = \left[\left(\frac{\Gamma D}{\sigma^* V k \Delta T_0} \right) \left(\frac{C_0}{C_i} \right) \right]^{1/2} \quad (11)$$

where σ^* is the dendrite tip selection parameter for steady state dendrite growth and ΔT_0 is the freezing range of the alloy. Substituting R into the above equation, gives

$$\lambda = \left[\frac{32\Gamma D k}{\sigma^*} \right]^{1/4} G^{-1/2} V^{-1/4} \Delta T_0^{1/4} \quad (12)$$

where $C_0 \approx C_i$ is taken for dendrite growth at low velocity.

For grain growth analysis:

Assuming that grain growth is diffusion controlled, driven by surface energy, and requires no nucleation, the rate of growth at a fixed temperature T is given by

$$\frac{dg}{dt} = \frac{\kappa_1}{2g} \exp\left(-\frac{Q}{RT}\right) \quad (13)$$

and grain size, g , after time t is

$$g^2 - g_0^2 = \kappa_1 t \exp\left(-\frac{Q}{RT}\right) \quad (14)$$

where g_0 is the initial size, κ_1 is a kinetic constant, and Q an activation energy. Here, temperature (T) and time (t) can be obtained from the thermal history, and it is now easy to predict grain growth history at the HAZ. Initial grain size can be obtained from experimental samples.

2.2. Materials data

Material properties often behave with non-linearity in high temperature regimes and should be properly dealt with in the governing equation. For instance, specific heat, thermal conductivity, elastic modulus, thermal expansion coefficient, and plastic modulus. etc., can be

varied with temperature. In this model, these material properties were treated as functions of temperature and, when necessary, data was interpolated. Since it is still not possible to get temperature dependent properties for solidification and grain growth, constants, or alternatives if properties were not available, were used.

The availability of thermo-physical data in the literature seemed to be limited. Most data was obtained from room temperature to 2/3 of the melting temperature. Above the melting range, a few experimental researchers produced useful data [57]. With the latent heat effect, the thermo-physical properties of 304 stainless steel demonstrate a sudden change at melting temperature. Due to this, thermal conductivity and diffusivity may be essential constants affecting the thermal history of the welding process. Expansion coefficients and specific heat also exhibit the change at melting temperature. The sudden increase enhances residual strain during the heating process. When the heat eventually drops, it causes the residual stress in the heat-affected area of the weldment.

The thermo-mechanical properties for AISI 304SS are limited in the range of operating temperatures. For instance, above 1/3 of the melting temperature (T_m), most metals experience creep, causing their mechanical properties to drop significantly, and making it difficult to estimate the value near melting point. Stainless steel is not an exception [58].

Most of the experimental data for solidification reported are based on pure component or binary alloy cases. AISI 304 stainless steel is a multicomponent alloy with Fe, Cr, Ni, and trace amounts of other elements, as shown in Table V. Thus, the data from similar binary alloy system (for instance, γ Fe-Ni binary alloy, or Fe-Cr binary phase diagram) was used as an alternative for the numerical work, as shown in Table VI. Some data, such as the Gibbs-Thomson coefficient (Γ)

TABLE V AISI 304 stainless steel typical composition

AISI type no.	Nominal composition (wt%)				
	C	Mn	Cr	Ni	Other (Fe, etc)
304	0.08 max	2.0	18–20	8.0–12	~70 Fe

TABLE VI Thermo-physical constants of AISI 304 SS for solidification analysis

Solidification constants	Value
$m_\alpha = \Delta T/\Delta C = \text{Solve of liquidus temperature (K/wt\%): for } \gamma\text{Fe-Ni}$	-2.4
$R_g = \text{Gas constant (J/mol} \cdot \text{K)}$	8.31
$D_0 = \text{Pre-exponential term (diffusion, m}^2\text{/s) for } \gamma\text{Fe-Ni}$	$7.50 \cdot 10^{-9}$
$Q = \text{Activation energy for diffusion (J/mol)}$	230.58
$\Gamma = \text{Gibbs-Thomson coeff. (solid-liquid interface energy}/\Delta\sigma_f, \text{ mK) for } \gamma\text{Fe}$	$1.90 \cdot 10^{-7}$
$\sigma^* = \text{Operating parameter for dendrite growth}$	$1/(4\pi^2)$
$\alpha_0 = \text{Atomic jump distance for partitioning coeff.}$	$4.0 \cdot 10^{-10}$
$k_0 = \text{Equilibrium partitioning coeff.}$	0.8
$C_0 = \text{Composition for Cr (72 wt\%Fe-18 wt\%Cr-10 wt\%Ni)}$	~18.
$C_t = \text{Dendrite tip composition}$	~18.

TABLE VII Physical constants for grain growth analysis

Constants	Value
g_0 = Initial grain size (mm)	$18.0 * 10^{-3}$
k_1 = Grain constant (mm^2/s)	$7.50 * 10^5$

and solid-liquid interface energy, were obtained from pure components (γFe) [59]. The data from pure or binary component materials may cause some errors in this modeling work. However, most solidification data applied for the numerical simulation could be reasonably close to that of AISI 304 stainless steel. There have been some discussions on the solidification constant with regard to the operating parameter (σ^*) for the dendrite growth [60, 61]. σ^* is the major constant which determines the shape of dendrite as well as the morphology of dendrite. For this analysis, $\sigma^* = 1/(4*\pi^2) = 0.0253$ has been used.

For the grain growth analysis, the constants shown in Table VII were used. In this case, it was hard to get the grain constant for AISI 304 stainless steel, since only Ashby and his fellows have done work in this area [28, 29, 62]. Some data was obtained from his early work.

2.3. Mathematical modeling

Most formulations and the basis of the finite element model for the heat transfer analysis can be found in previous works [25, 58]. For stress analysis, the thermal history obtained from heat transfer analysis was used as an initial condition. For solidification analysis, the temperature history from the heat transfer analysis was modified and utilized using an algorithm developed for this analysis. The algorithm was adapted to incorporate marginal stability theory as well as steady-state dendrite growth theory. Diffusion coefficients as well as partitioning coefficients were used as temperature-dependent values. The grain size at the HAZ was also predicted by using the diffusion control model. It was assumed by Ashby that the diffusion is driven by surface energy, and no nucleation is required [28, 29]. This grain growth model then adapts the extent of transformation, which depends on the integrated number of diffusive jumps during weld cycles.

3. Results and discussion

3.1. Heat transfer analysis

Heating and cooling are the key process in welding, causing complex and severe phenomena in the welding microstructure. Fig. 3 shows the temperature history at $x = 25.4$ mm plane. (Welding power = 6 kW, welding speed = 3.39 mm/sec) (a) $t = 8.9$ sec (b) $t = 9.3$ sec (c) $t = 10.0$ sec, and (d) $t = 10.2$ sec for $y = 0$ plane. The melting range can be detected from the solidus and liquidus temperature. Fig. 3a shows the temperature isotherm after the torch is turned off at $t = 7.5$ sec. From this contour, one can also predict the width to depth ratio of the FZ. After $t = 10.2$ sec, as shown in Fig. 3d, there is no longer a melting zone.

For cooling rate information, which is important in determining the solidification history, Fig. 4 was constructed. It shows the cooling rate history at $y = 3.4$ mm plane, parallel to the welding direction. As shown in Fig. 4, negative means heating, while positive means cooling. This shows that the maximum cooling rate during the process is about an order of 10^3 °C/sec, and the cooling rate decreases drastically once the heat source is gone.

3.2. Solidification analysis

Temperature history from heat transfer analysis is used as an input to calculate the solidification variables such as temperature gradient, cooling rate, and growth rate. In this modeling, the Scheil equation [63] or non-equilibrium lever rule for solute redistribution was employed, since solid state diffusion is small. Complete mixing is assumed to occur in the liquid. The assumption would be valid for primary austenite solidification where the diffusion rates are certainly low enough.

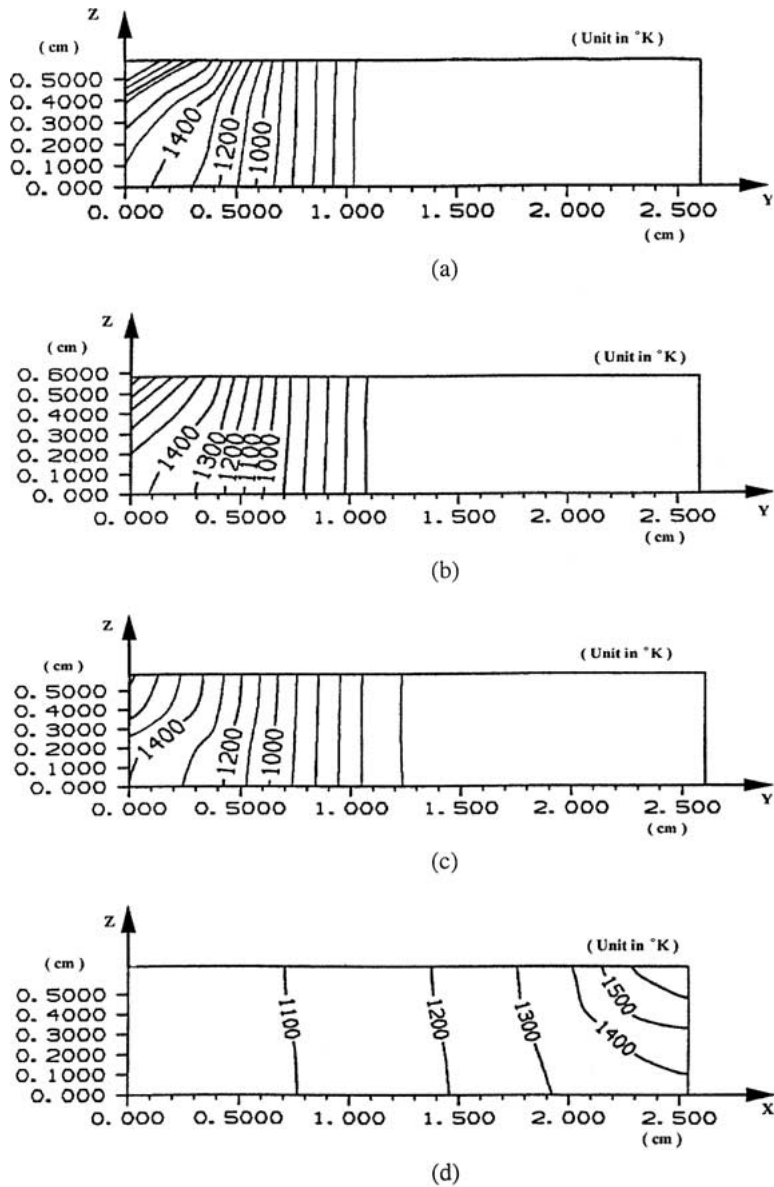
Since nucleation kinetics was not considered in this model, the prediction of the solidification history is incomplete. However, solidification in the weld does not necessarily require nucleation before growth of the solid interface since the liquid atoms need only assume positions corresponding to extension of the crystal lattice of the solid [64]. Nevertheless, the predicted PDAS match well with the measured PDAS in both columnar and equiaxed dendrites. Mainly, the PDAS was investigated because it can be easily verified through experimentation. The secondary dendrite arm spacing (SDAS) and tip radius, as a by-product, were not extensively measured in the experiment.

Fig. 5 shows the temperature history at $x = 0$ plane when (a) $t = 1.5$ sec, (b) $t = 2.2$ sec, and (c) $t = 2.8$ sec. Based on the temperature information (Fig. 6 for the 821 node case), a solidification history was constructed. The movement of the solidification front, which is nearly identical to the isotherm, controls the solidification speed, which results in microstructure evolution.

Fig. 7 simulates the solidification variables in different positions along depth from the top surface at the FZ. From the simulation, one can find that the solidification speed is not constant, but changes with time and usually tends to decrease at the end of solidification. It is noted that the advantage of the transient model can be characterized and strengthened from these figures.

Fig. 8 plotted the predicted PDAS contour after solidification completed in the $v = 3.39$ mm/sec case. The PDAS at the interface appeared shorter than that in the center area of the FZ, even though the solidification velocity in the center area at the FZ is higher than that at the interface. It was explained that the effect of temperature gradient on PDAS was much greater than that of solidification speed. The observed differences here are caused mainly by differences in temperature gradient variations, where temperature gradient is much higher at the fusion line than at the weld center line.

The analysis for dendrite growth was performed using the formulations based on the Hunt-Trivedi model. The results show that the variation during solidification



(Note: horizontal axis is y axis for (a), (b), (c), and x axis for (d)
(unit in cm for x,y and z axis, unit in °K for temperature)

Figure 3 Temperature contour history (Welding power = 6 kW, welding speed = 3.39 mm/sec) (a) $t = 8.9$ sec (b) $t = 9.3$ sec (c) $t = 10.0$ sec for $x = 25.4$ mm plane, and (d) 10.2 sec for $y = 0$ plane, where $t =$ accumulated heat transfer time.

time exists, and it is approximately within an order of magnitude. The temperature gradient was generally in an order of 10^4 – 10^5 K/m, while solidification speed appeared within an order of 10^{-2} to 10^{-3} m/sec. The PDAS was in the range of 10^1 to 10^2 μm . The range of the sizes was in good agreement with the values in the references [59–65].

The influence of welding speed on the PDAS was also simulated as shown in Fig. 9. As expected, the PDAS decreases with increasing welding speed. It is noted that the range of the PDAS, i.e. the growth of spacing during solidification, varies with the welding speed.

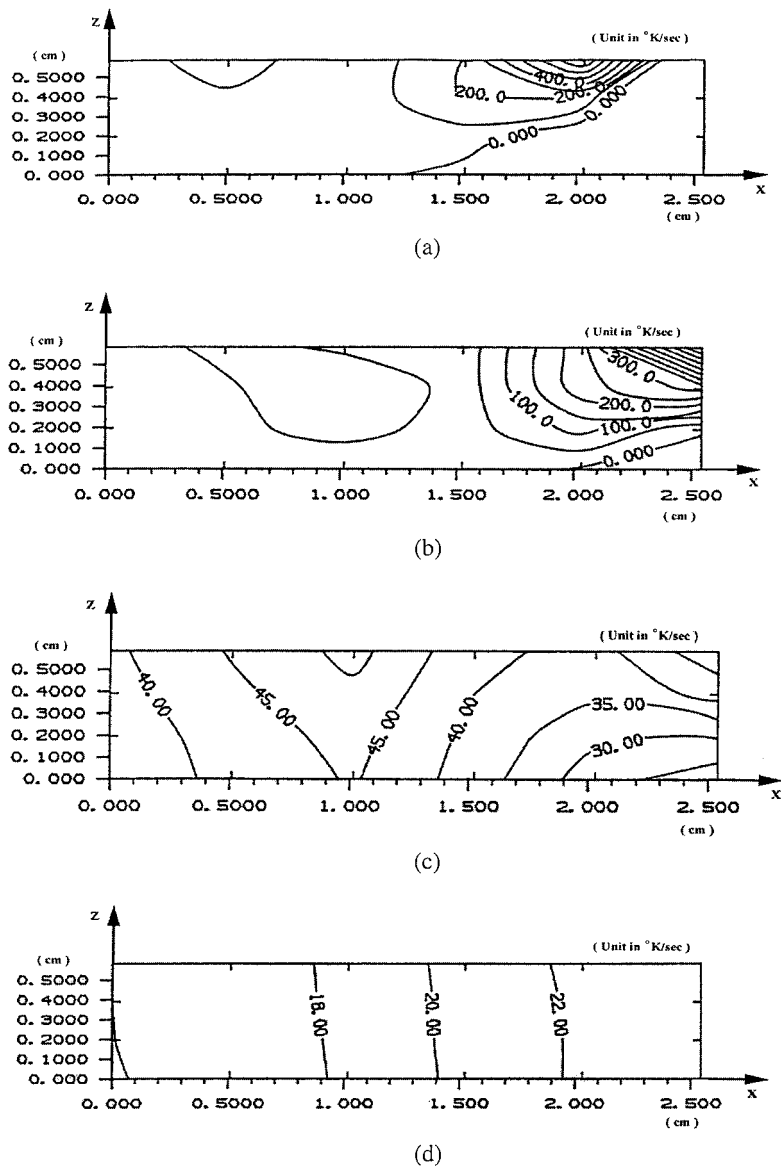
3.3. Stress analysis

Fig. 10 shows the residual stress distribution at the $x = 0$ plane. As shown in the figures, the residual stresses after

$t = 7.0$ sec, when the heat source is removed, were low because the temperature was still high. However, it increased dramatically after $t = 1750$ sec. The stress state at the top surface ($y = 0$ plane) shows a large amount of residual stress. At the top surface, the residual stress exceeded the yield stress (~ 280 MPa for 304 stainless steel).

Fig. 11a through c shows the simulation of the deformation structure history for this analysis. Stress and deformation are largely opposed. From the simulation, it can be predicted whether the magnitude of distortion is within the tolerance allowed, since the welding problems usually come from the over-distorted area due to improper welding process parameters.

Residual stresses in the longitudinal direction of the weld, in the transverse direction, and in the direction of plate thickness occur as a result of similar mechanisms. Weld-longitudinal stresses (S_{11}) are generated in



(unit in cm for x and z axis, unit in °K/sec for cooling rate)

Figure 4 Cooling rate contour history at $y = 3.4$ mm plane (welding power = 6 kW, welding speed = 5.08 mm/sec) (a) $t = 5$ sec (b) $t = 6$ sec (c) $t = 10$ sec, and (d) $t = 20$ sec where $t =$ accumulated heat transfer time.

accordance with the mechanism of a weld seam, which contracts longitudinally. The tensile stresses are limited to a narrow area close to the weld, their maximum value being at or above the yield limit. Lower compressive stresses exist in the surrounding region, dropping off rapidly the further away they are from the weld. Weld-transverse stresses (S_{22}) in the plane of the plate are generated in accordance with the mechanism of a weld seam which contracts transversely, especially when the plate is restrained. They are not restricted to a narrow area close to the weld, thus they exist in the surrounding region. They are supported in a similar way as external forces and, provided the support has sufficient elasticity, remain below the yield limit. Weld-transverse stresses in the direction of plate thickness (S_{33}) may at least then be generated if the plate thickness is sufficiently large. They result in the unsafe triaxial tensile stress states.

Fig. 12a and b show results for the predicted residual stresses for various welding speeds. Fig. 12a and b show the stress history at $v = 3.39$ mm/sec, and

$v = 5.08$ mm/sec, respectively. With increasing welding speed, the residual stresses appear to increase, since the cooling rate increases in the same fashion. As expected, the cooling rate appears to be the dominating factor in controlling the residual stress status.

3.4. Effect of cooling rate on stress in the FZ and HAZ

Welding speed is one of many welding process parameters that can change the microstructural characteristics. Cooling rate is strongly dependent upon the welding speed. If the welding speed increases, the cooling rate also increases. Increasing the welding speed decreases the total specific energy into the substrate. Most microstructural characteristics, including the PDAS and tip radius, are affected by the cooling rate change. Fig. 13 shows similar results, but at the FZ. Transient transverse stress (S_{22}) increased with increasing welding speed (compare (a) with (b)). Thus, the final residual

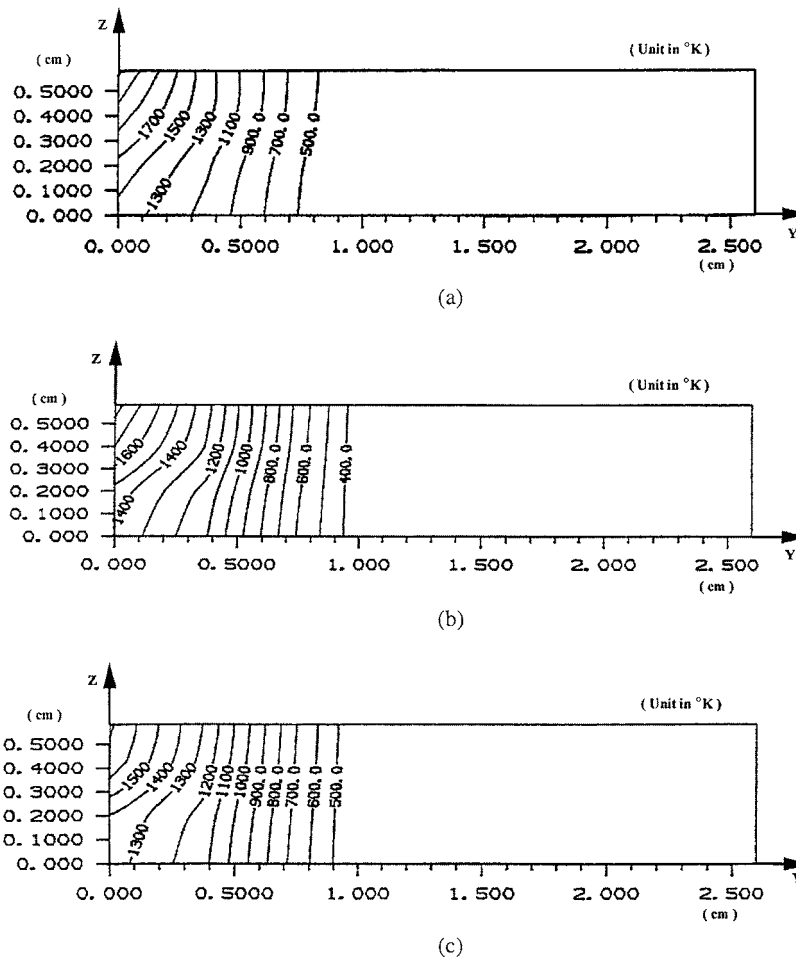


Figure 5 Temperature history at $x=0$ plane (welding power = 6 kW, welding speed = 5.08 mm/sec) (a) $t = 1.5$ sec, (b) $t = 2.2$ sec and (c) $t = 2.8$ sec.

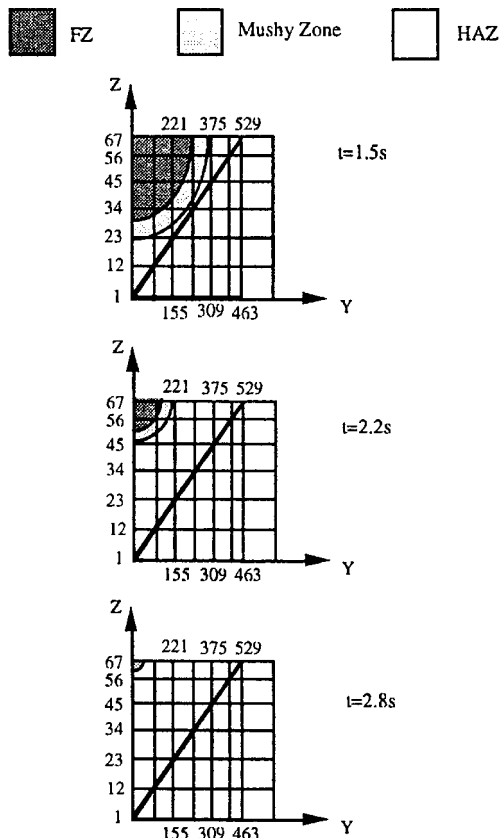


Figure 6 Solidification history at $x=0$ plane (821 nodes case) (welding power = 6 kW, welding speed = 5.08 mm/sec).

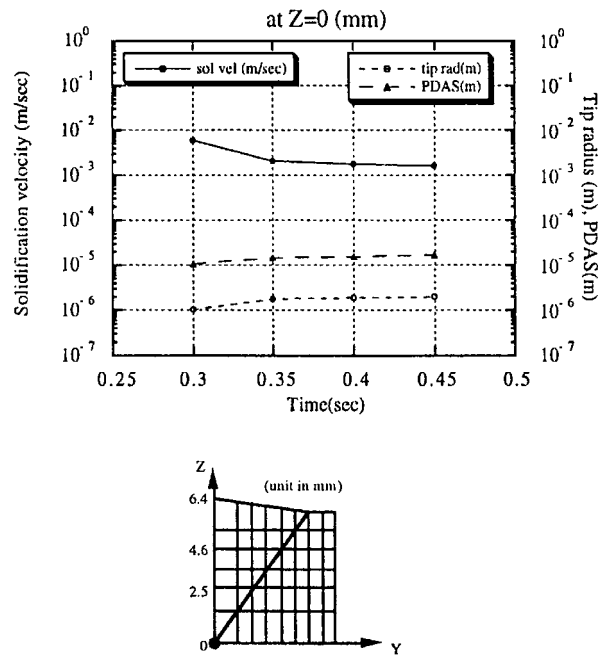


Figure 7 Microstructure history at $z=0$ mm (at $x=0$ plane).

stress of $v = 5.08$ mm/sec case will be higher than that of $v = 3.39$ mm/sec.

3.5. Effect of cooling rate on PDAS in the FZ
Influence of welding speed on the PDAS also was simulated as already shown in Fig. 9. It was observed that

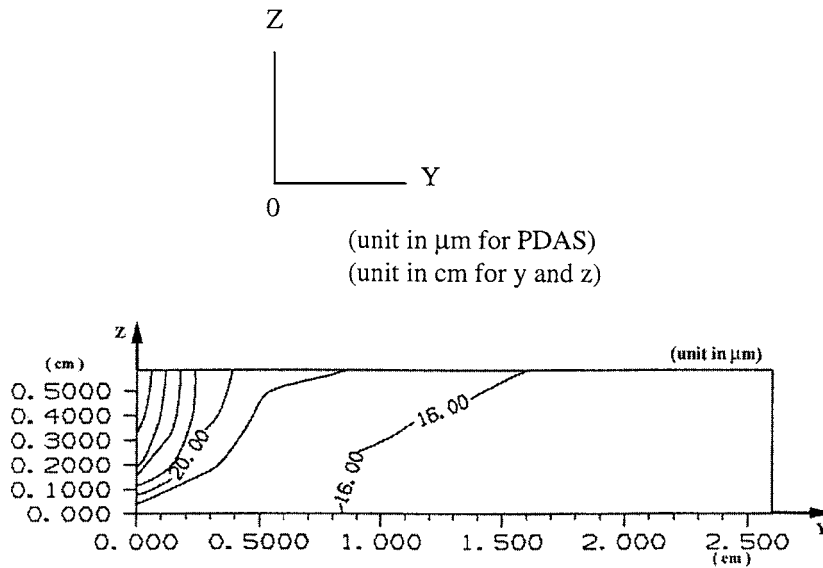


Figure 8 Predicted PDAS contour after solidification (at $x = 25.4$ plane) (welding power = 6 kW, welding speed = 3.39 mm/sec).

TABLE VIII Effect of process parameters on temperature-stress-microstructure fields

Fields	Variables	Trends			
Process parameters	Weld speed ^a (v)	↑	↓		
	Heat flux ^b (VI)			↑	↓
Temperature field	Power density (P)	↓	↑	↑	↓
	Cooling rate (dT/dt)	↑	↓	↓	↑
Stress field	Residual stress (σ)	↑	↓	↓	↑
	Residual strain (ϵ)	↑	↓	↓	↑
Microstructure field	PDAS, SDAS, r_{tip} (at FZ)	↓	↑	↑	↓
	Grain size (at HAZ)	↓	↑	↑	↓

^aWelding speed: 3.39 mm/sec, 5.08 mm/sec, and 7.62 mm/sec.

^bHeat flux: 4000 W and 6000 W.

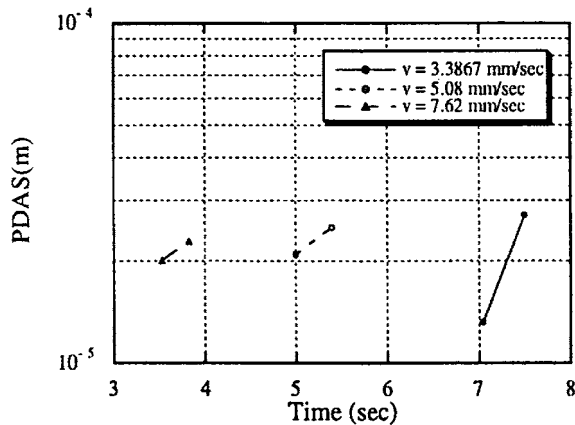


Figure 9 Simulated PDAS vs. welding speed (v) during solidification (welding power = 6 kW, at the FZ ($x = 15.24$, $y = 0$, $z = 6.24$), unit in mm).

higher welding speeds result in shorter PDAS. It is noted that the range of PDAS, i.e. the growth of spacing during solidification, varies with the welding speed. Since cooling rate is related to welding speed, it is natural that the PDAS shortens with higher welding speeds.

Table VIII summarizes the relationship between the three welding fields and process parameters. Increasing weld speed and decreasing weld heat flux will increase the cooling rate. Increasing the cooling rate will result in an increase of residual stress and strain. Meanwhile,

one can expect narrow PDAS and SDAS with increasing cooling rate.

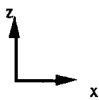
3.6. Experimental verification

Experimental temperature and strain measurements have been performed using thermocouples and strain gages with automatic data acquisition systems. Fig. 14 shows the experimental set-up for this welding experiment. A process controller and a temperature data acquisition device were used to collect transient temperature data with thermocouples. Strain data was collected separately through a strain data acquisition device with strain gages. The welding machine with an image processing CCD camera was operated under a computer controlled system. The machine had 2 axes (x and y) controlled by a computer and one, the z -axis, controlled manually.

Welding samples were prepared with thermocouples and strain gages, which were mounted on the surface (top and bottom). For strain data collection, the SOMAT[†] data acquisition system was employed since the system can collect and plot the transient data with good sampling resolution and a well-designed noise protection device. The data acquisition stacks are properly arranged to protect from the possible noise. The strain gages were so sensitive and fragile that excessive heat from radiation during the GMAW process could cause severe damage to the gage wire as well as the strain gage itself (Diameter = 1.5875 mm, Max. Temp. allowed 750°F). To protect the gage from the radiation heat, RTV (Room Temperature Volcano) coating was used to the gages. The strain acquisition device was also synchronized with the weld system controller so that all of the data can be gathered in the same fashion. (Table IX)

SEM photo images of the FZ, as shown in Fig. 15a and b, reveal the size of columnar and equiaxed dendrite, respectively. The transition zone between

[†] SOMAT[®] is a trademark of SOMAT Inc. in Champaign, Illinois.


 (unit in cm for x and z axis and MPa for stress)

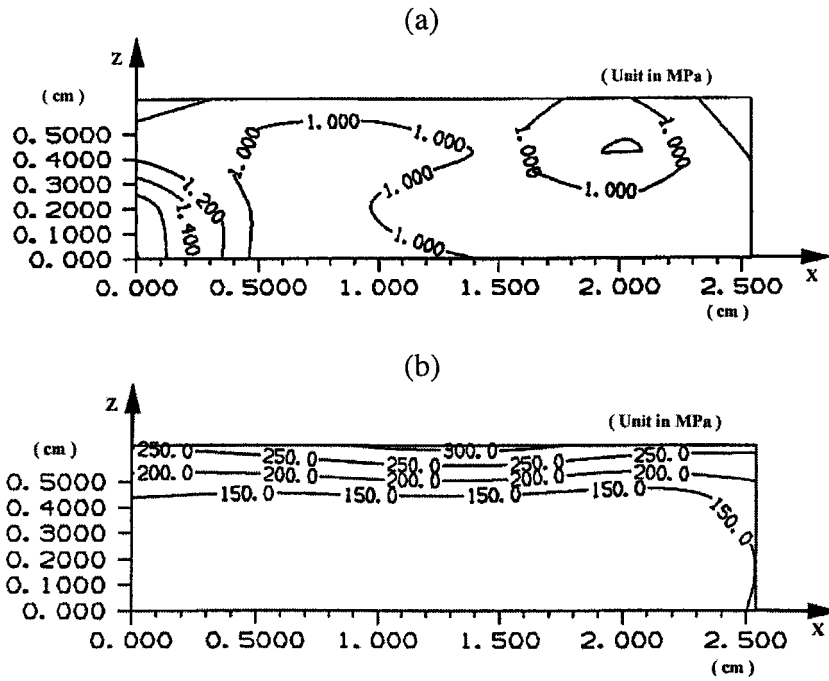


Figure 10 Residual stress (Von Mises stress) distribution at $y = 0$ plane (a) after 7 sec, (b) after 1750 sec (welding power = 6 kW, welding speed = 5.08 mm/sec).

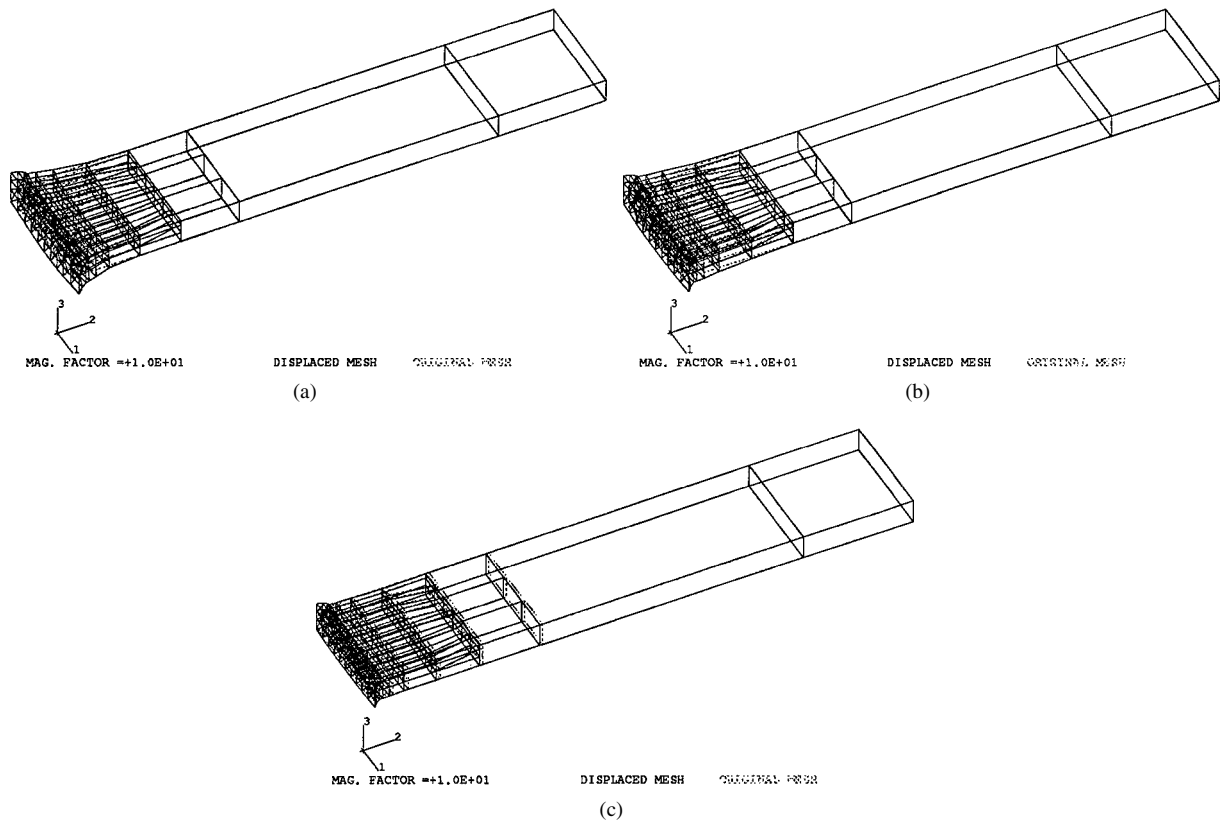
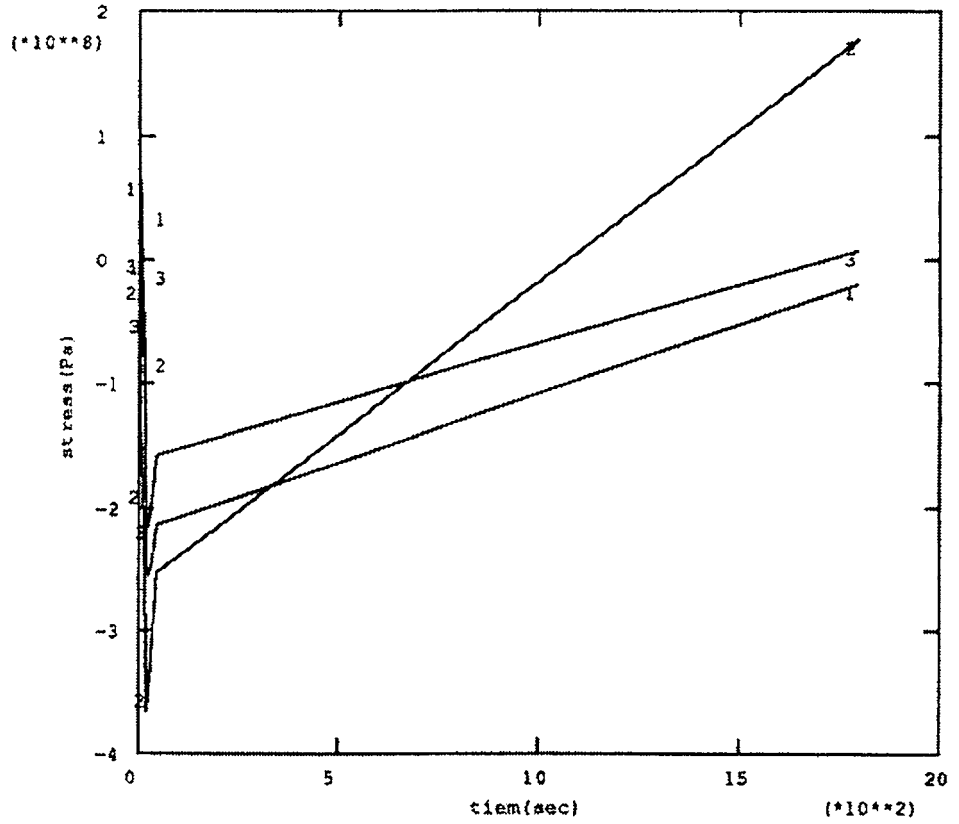


Figure 11 Deformed shape history (welding power = 6 kW, welding speed = 5.08 mm/sec) (a) $t = 6.2$ sec, (b) $t = 20.0$ sec, and (c) $t = 1800.0$ sec (magnification factor = 10).

LINE	VARIABLE	SCALE FACTOR
1	#11 (EL225)	+1.00E+00
2	#22 (EL225)	+1.00E+00
3	#33 (EL225)	+1.00E+00



LINE	VARIABLE	SCALE FACTOR
1	#11 (EL225)	+1.50E+00
2	#22 (EL225)	+1.50E+00
3	#33 (EL225)	+1.50E+00

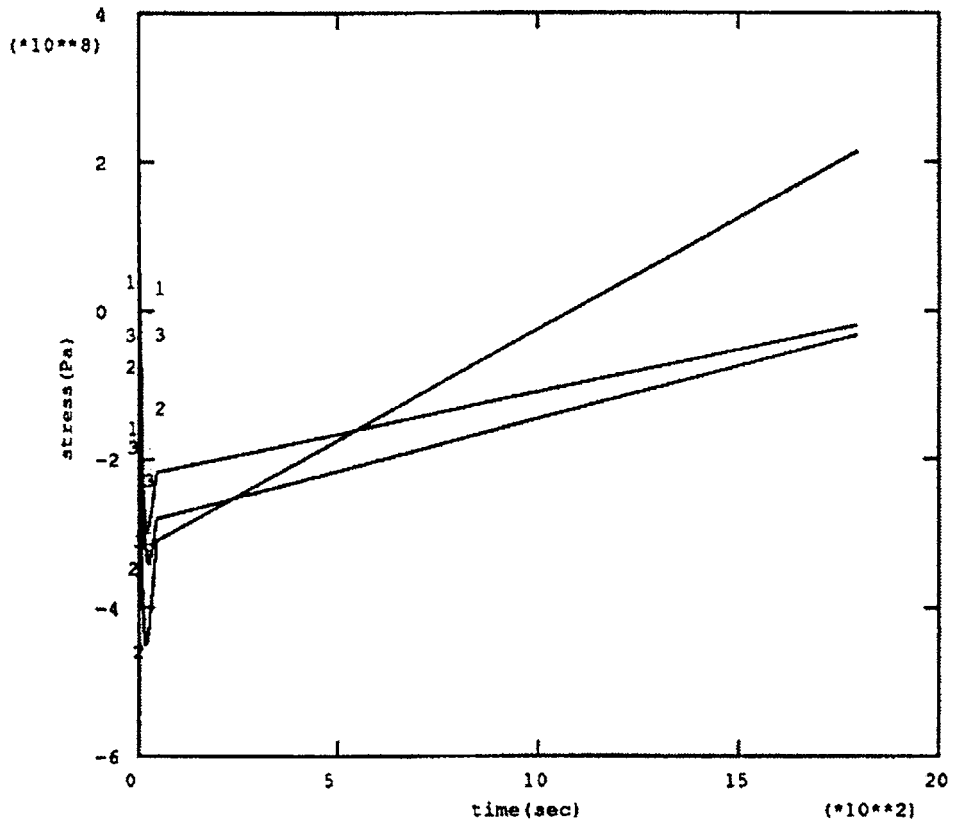
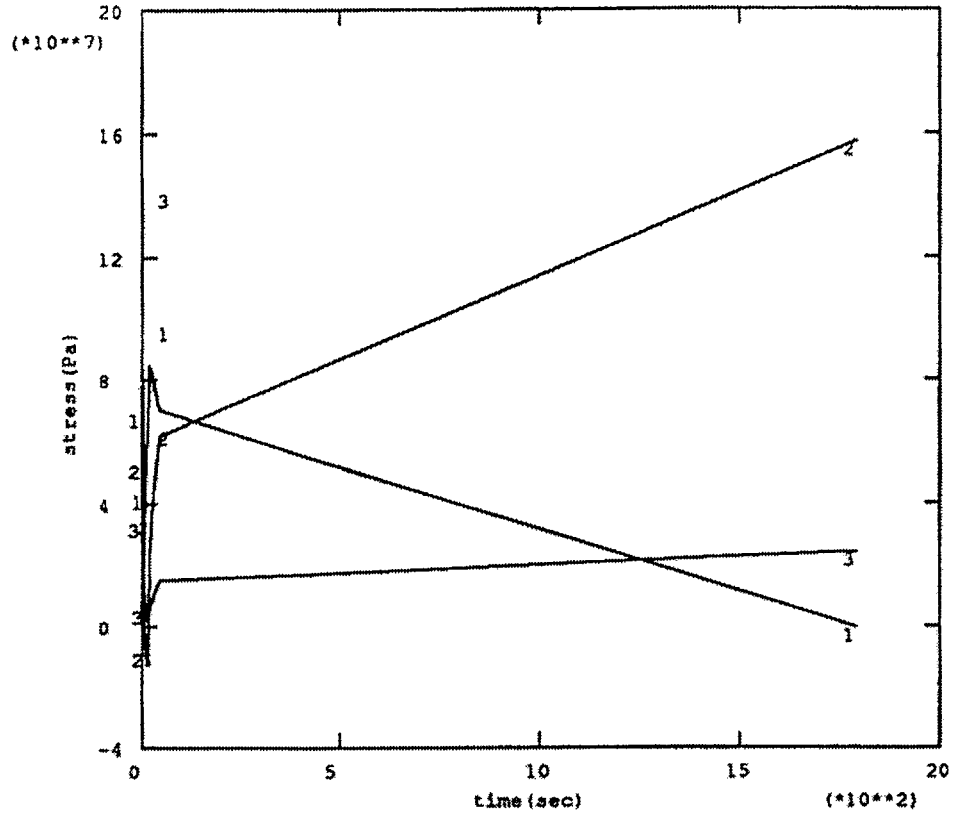


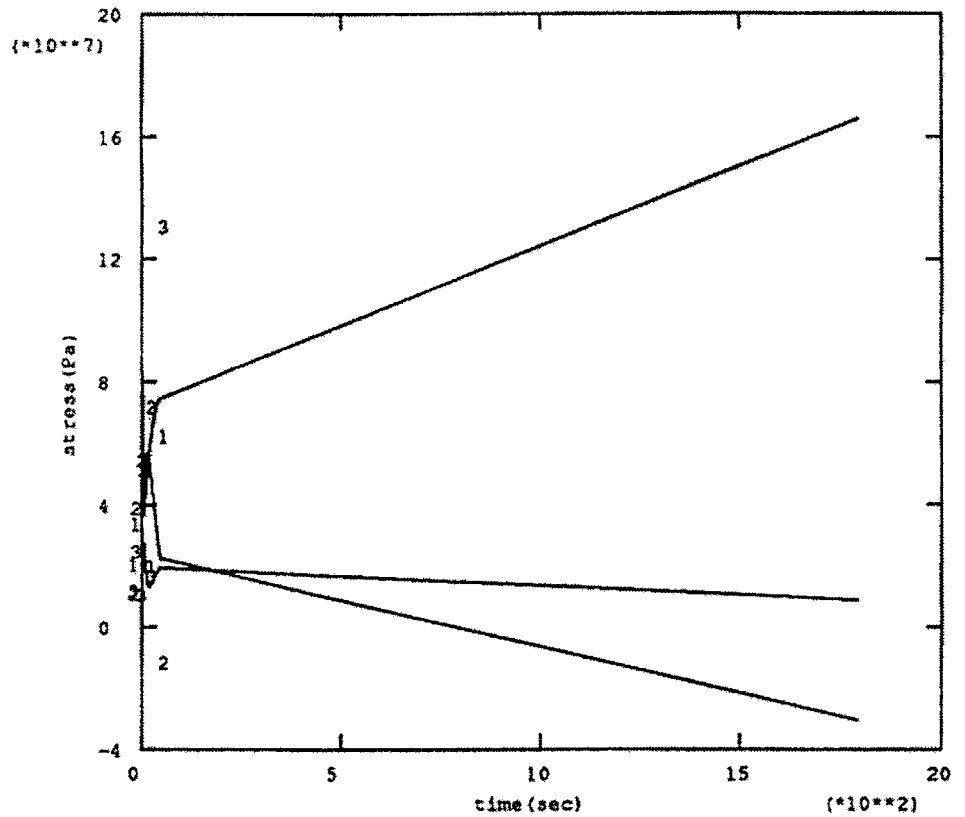
Figure 12 Predicted residual stress history for various welding speeds (a) $v = 3.39$ mm/sec, (b) $v = 5.08$ mm/sec.

LINE	VARIABLE	SCALE FACTOR
1	#11 (EL035)	+1.00E+00
2	#22 (EL035)	+1.00E+00
3	#33 (EL035)	+1.00E+00



(a)

LINE	VARIABLE	SCALE FACTOR
1	#11 (EL035)	+1.00E+00
2	#22 (EL035)	+1.00E+00
3	#33 (EL035)	+1.00E+00



(b)

Figure 13 Effect of welding speed on residual stresses at FZ. (a) $v = 3.39$ mm/sec, and (b) $v = 5.08$ mm/sec.

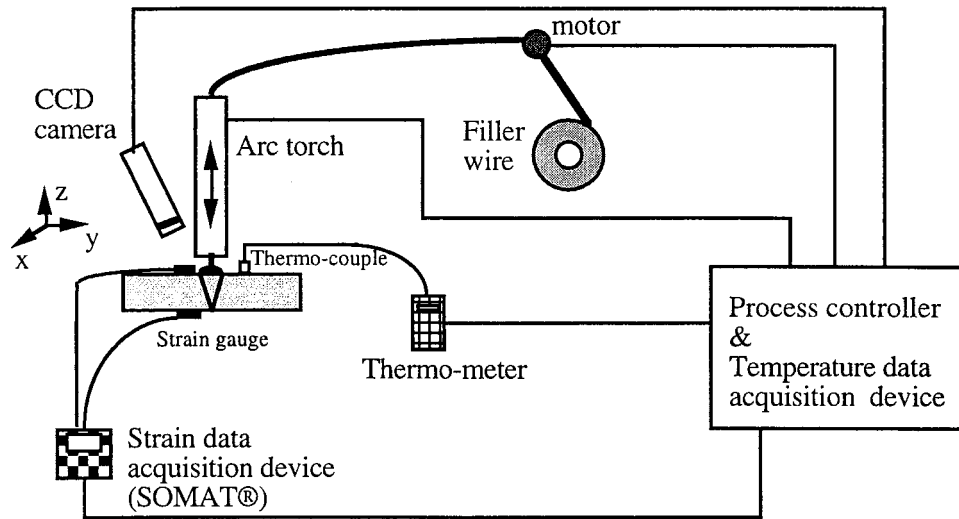


Figure 14 Experimental set-up for GMAW.

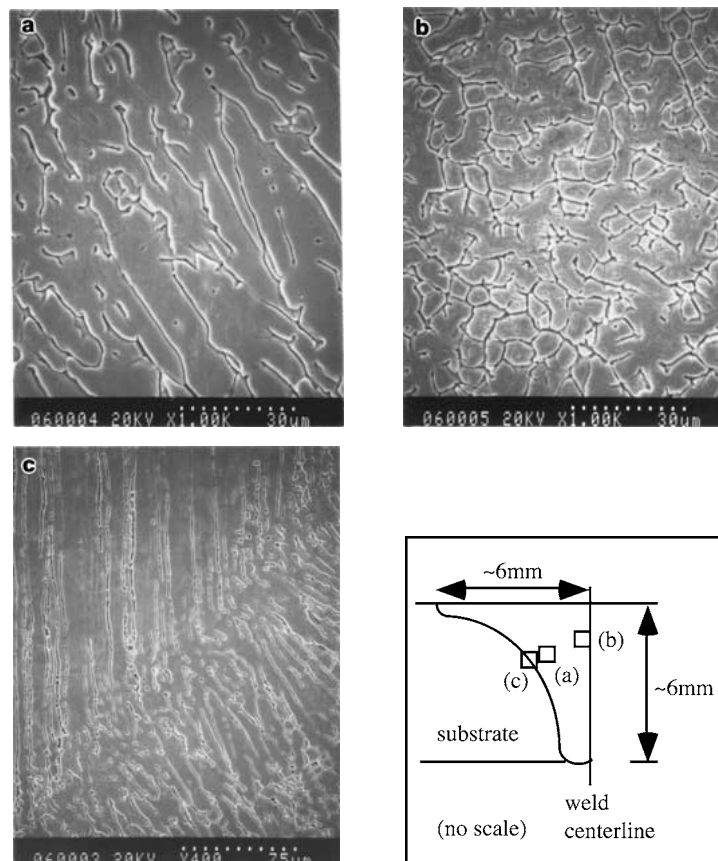


Figure 15 SEM image at FZ (sample#6) (a) columnar dendrite zone, (b) equiaxed dendrite zone, (c) transition zone.

columnar and equiaxed dendrites, in general, appears in the mixed dendrite zone, as shown in Fig. 15c.

The experimental results are very much in accord with earlier simulated results. Fig. 16 shows the comparison between simulated results and experimental results for welding power = 6 kW and speed = 5.08 mm/sec at the HAZ.

Fig. 17 shows the comparison of experimental data with predicted data generated by this modeling work. At the FZ, both columnar and equiaxed dendrites show small gaps between the predicted data and the experimental data measured, but they remain in the same order

of magnitude. The predicted data from the numerical model show slightly higher values than the data from the experiment, but they are within an order of magnitude.

Columnar dendrites, which are oriented toward the FZ from the interface of the FZ and the HAZ, show very uniform distribution throughout the FZ. The average columnar dendrite size was dependent upon the welding speed and measured between about 7.5 to 20 μm for welding speeds of 3.39 to 7.62 mm/sec. Even though the predicted one has a little bit higher value than experimental one, the difference is within an order of magnitude.

TABLE IX Strain/temperature data set

Sample no.	Power (kW)	Speed (mm/sec)	Strain gage position from center (mm)
welds1	6	7.62	16
welds2	6	5.08	25
welds3	6	5.08	40
welds#1	6	5.08	16
welds#2	6	5.08	25
welds#3	6	5.08	40
welds#4	6	7.62	16
welds#5	6	7.62	25
welds#6	6	7.62	40
welds#7	6	3.39	16
welds#8	6	5.08	25
welds#9	6	5.08	40

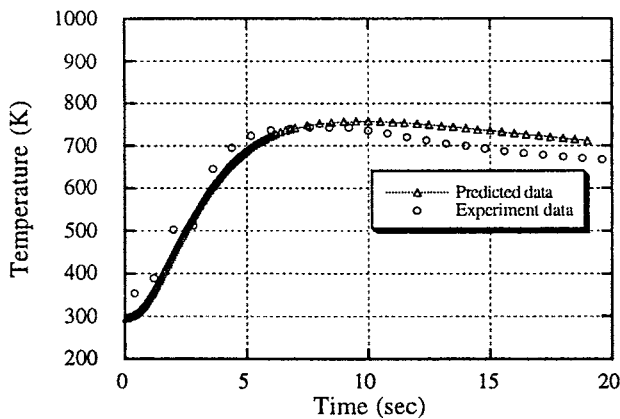


Figure 16 Comparison of predicted and experiment data at HAZ (welding power = 6 kW, welding speed = 5.08 mm/sec) ($y = 16$ mm from weld centerline at top surface).

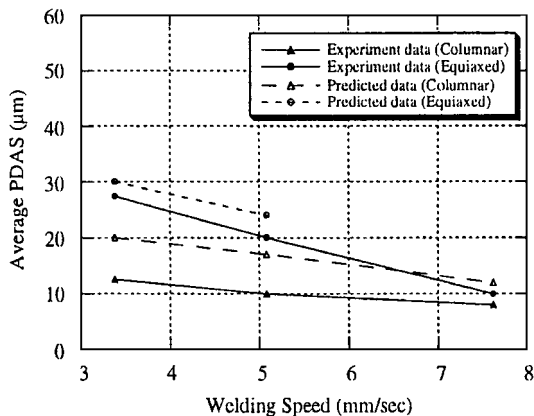


Figure 17 Comparison of numerical and experimental data (welding power = 6 kW).

Equiaxed dendrites, which are observed in the central part of the FZ, show closer agreement with predicted data. The average size of the equiaxed dendrites was also dependent upon the welding speeds and measured between 10 to 30 μm for welding speeds of 3.39 to 7.62 mm/sec. It should be noted that increasing the welding speed decreases the size of the PDAS as well as the SDAS.

Fig. 18 shows the comparison of numerical and experimental strain data at $y = 25$ mm on the top surface

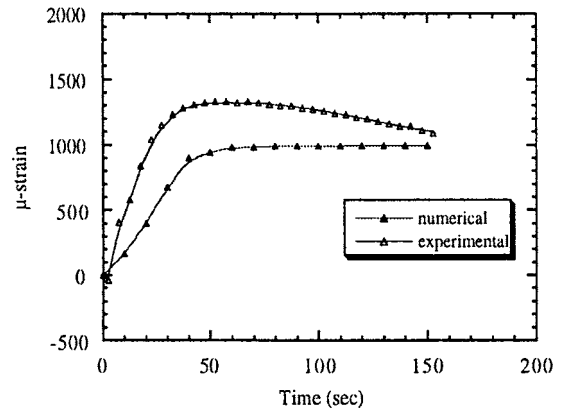


Figure 18 Comparison of numerical and experimental total strain (ϵ_{22}) data ($y = 25$ mm at top surface: ($x = 8.46$ mm, $y = 25.0$ mm, $z = 5.82$ mm)) (welding power = 6 kW, welding speed = 5.08 mm/sec).

[($x = 8.46$, $y = 25.0$, $z = 5.82$): unit in mm]. The numerical strain data shows lower transient strain than the experimental data (about 10–20% lower). Since the model does not consider phase transformation stress after solidification, the numerical data could be smaller than that of the experiment. Adding creep analysis into the stress model may help improve prediction since excessive heat energy could contribute to the creep phenomena during the cooling cycle of the welding process. In addition, one can explain that the difference is due to the accuracy of thermomechanical data employed in the model.

As a result, the experimental results prove the model prediction of this work is reasonably close to the real case. The assumptions made during the course of modeling are reasonable in retrospect. Nevertheless, the model could be made better by the addition of a phase transformation analysis. Surely the experimental verification makes this model powerful and reliable.

4. Conclusion

In summary, networking three weld fields—temperature, microstructure, and stress—has been attempted and produced a reliable model using a numerical method with the finite element analysis technique. Experimental results have validated this modeling effort. The effect of the welding process parameters to the welding fields was analyzed and reported. It has been suggested that perhaps the specific welding energy (welding power/welding speed) is the controlling parameter for the welding process in determining the three weld fields. This implies that increasing the welding power and welding speed will give the same results as decreasing the welding power and welding speed in the thermal, stress and microstructure distributions. However, this could not be verified since welding power was not varied in the experiments. In the future, these problems should be addressed. The effort to correlate residual stress and the microstructure field has been initiated and some valuable results have been found.

Acknowledgment

This work was made possible by grants from the U.S. Department of Defense. FEM of heat transfer and stress field was supported by a grant from Army Research Office/Advanced Construction Technology Center at the University of Illinois at Urbana-Champaign. (Grant No. DAAL03-87-K-0006) The microstructure modeling work was supported by a grant from ONR (Grant No. N00014-89-J-1473). We would also like to express our sincere thanks to Bob Weber of the U.S. Army Construction Engineering Research Laboratories, Champaign, Illinois.

References

1. D. ROSENTHAL, *Welding J.* **20** (1941) 220s.
2. *Idem.*, *Trans. ASME* **68** (1946) 849.
3. P. S. MYERS, O. A. UYEHARA and G. L. BORMAN, *Welding Research Council Bulletin* **123** (1967) 1.
4. D. R. ATHEY, *J. Fluid Mech.* **98**(4) (1980) 787.
5. G. M. OREPER and J. SZEKELY, *ibid.* **147** (1984) 53.
6. C. CHAN, J. MAZUMDER and M. M. CHEN, *Met. Trans. A* **15** (1984) 2175.
7. S. KOU and D. K. SUN, *ibid.* **16** (1985) 203.
8. S. KOU and Y. H. WANG, *ibid.* **17** (1986) 2265.
9. *Idem.*, *Weld. J.* **64** (1986) 63s.
10. C. CHAN, J. MAZUMDER and M. M. CHEN, *Mat. Sci. and Tech.* **3** (1987) 306.
11. *Idem.*, *J. Appl. Phys.* **64**(11) (1988) 6166.
12. T. ZACHARIA, A. H. ERASLAN, D. K. ALDUN and S. A. DAVID, *Met. Trans. B* **20** (1989) 645.
13. R. ZEHR, Ph.D. thesis, University of Illinois at Urbana-Champaign, 1991.
14. R. DUCHARME, K. WILLIAMS and P. KAPADIA, in Proceedings of ICALEO 1993, edited by P. Denney, L. Miyamoto and B. L. Mordike (LIA, Orlando, 1993) p. 97.
15. H. D. HIBBITT and P. V. MARCAL, *Computers and Structures* **3** (1973) 1145.
16. E. FRIEDMAN, *J. Press. Vessel Tech. (Trans. ASME)* **8** (1975) 206.
17. B. A. B. ANDERSSON, *Trans. ASME, J. of Eng. Materials and Technology* **100** (1978) 56.
18. E. F. RYBICKI, in "Welding: Theory and Practice," edited by D. L. Olson, R. Dixon and A. L. Liby (North-Holland, Amsterdam, 1990) p. 325.
19. B. ANDERSSON and L. KARLSSON, *J. of Thermal Stresses* **4** (1981) 491.
20. J. H. ARGYRIS, J. SZIMMAT and K. J. WILLIAM, in "Computer Methods in Applied Mechanics and Engineer" (North-Holland, New York, 1982) p. 635.
21. M. C. STITT, MS thesis, University of Illinois at Urbana-Champaign, 1983.
22. J. GOLDAK, M. BIBBY, J. MOORE, R. HOUSE and B. PATEL, *Met. Trans. B.* **17** (1986) 587.
23. K. W. MAHIN, W. WINTERS, T. M. HOLDEN and S. R. MACEWEN, *Welding J.* **70** (1991) 245.
24. E. PARDO and D. C. WECKMAN, *Met. Trans. B.* **20B** (1989) 937.
25. P. K. TEKRIWAL, Ph.D. thesis, University of Illinois at Urbana-Champaign, 1989.
26. A. PAUL and T. DEBROY, "Advances in Welding Science and Technology" edited by S. A. David (ASM International, Metals Park, OH, 1987) p. 29.
27. P. TEKRIWAL and J. MAZUMDER, "Optimization of Welding Processes Using a Mathematical Model," US Army Const. Eng. Res. Lab., 1984.
28. M. F. ASHBY and K. F. EASTERING, *Acta Metall.* **30** (1982) 1969.
29. J. C. ION, K. E. EASTERING and M. F. ASHBY, *ibid.* **32** (1984) 1949.
30. J. S. KIRKALDY and D. VENUGOPALAN, in "Phase Transformation in Ferrous Alloys," edited by A. R. Marder and J. J. Goldenstein (Am. Inst. Min. Engrs., 1984) p. 125.
31. H. G. KRAUS, *Welding J.* **68** (1989) 269s.
32. A. PAPAPETROU, *Zeitschrift für Kristallographie* **92** (1935) 89.
33. G. P. IVANTSOV, *Dokl. Akad. Nauk SSSR* **58** (1947) 567.
34. W. W. MULLINS and R. F. SEKERKA, *J. Appl. Phys.* **34** (1963) 323.
35. *Idem.*, *ibid.* **35** (1964) 444.
36. V. V. VORONKOV, *Sov. Phys. Solid. St.* **6** (1964) 2378.
37. K. A. JACKSON and J. D. HUNT, *Trans. AIME* **236** (1966) 1129.
38. W. OLDFIELD, *Mat. Sci. Engr.* **11** (1973) 211.
39. J. S. LANGER and H. MÜLLER-KRUMBHAAR, *Acta Metall.* **26** (1978) 1681, 1689, 1697.
40. J. D. HUNT, in "Solidification and Casting of Metals," Book 192 (The Metals Society, London, 1979) p. 3.
41. W. KURZ and D. J. FISHER, *Acta Metall.* **29** (1981) 11.
42. R. TRIVEDI, *Met. Trans. A* **15A** (1984) 977.
43. P. MAGNIN and R. TRIVEDI, *Acta Metall. Mater.* **39** (1991) 453.
44. J. LIPTON, M. E. GLICKMAN and W. KURZ, *Met. Trans. A* **18** (1987) 341.
45. B. CARRUPT, M. RAPPAPAZ and M. ZIMMERMANN, in Proceedings of IVth Conf. on Modeling of Casting and Welding Process, edited by G. J. Abbaschian and A. F. Giamei (The Minerals, Metals, & Materials Society, Palm Coast, FL and Warrendale, PA, 1988) p. 581.
46. M. RAPPAPAZ and V. VOLLER, *Met. Trans. A* **21** (1990) 749.
47. R. TRIVEDI and W. KURZ, *ibid.* **21** (1990) 1311.
48. M. RAPPAPAZ, *Int. Mat. Rev.* **34** (1989) 93.
49. M. RAPPAPAZ and D. M. STEFANESCU, "Solidification Processing of Eutectic Alloys," edited by D. M. Stefanescu (Metallurgical Soc. of AIME, Warrendale, PA, 1988) p. 133.
50. C. S. KANETKAR, D. M. STEFANESCU, N. EL-KADDAH and G. CHEN, "Solidification Processing" (The Institute of Metals, London, 1988) p. 503.
51. M. RAPPAPAZ and P. THEVOZ, *Acta Metall.* **35** (1987) 1487.
52. A. F. GIAMEI, *JOM* **45** (1993) 51.
53. J. A. BROOKS, M. I. BASKES and F. A. GREULICH, *Metall. Trans. A: Phy. Metall. Mat. Sci.* **22** (1991) 915.
54. D. F. WATT, L. COON, M. BIBBY, J. GOLDAK and H. C., *Acta Metall.* **36** (1988) 3029.
55. W. PRAGER, *J. Appl. Mech.* **23** (1956) 493.
56. H. Q. ZIEGLER, *Appl. Math.* **17** (1959) 55.
57. C. S. KIM, "Thermophysical Properties of Stainless Steel," Argonne National Laboratory, ANL-75-25, 1975.
58. J. CHOI, Ph.D. thesis, University of Illinois at Urbana-Champaign, 1994.
59. W. KURZ and D. J. FISHER, "Fundamental of Solidification," (Trans Tech Pub., Aedermannsdorf, Switzerland, 1986) p. 242.
60. J. S. LANGER, in Indo-US Workshops on Solidification Principles and Materials Processing, edited by R. Trivedi, J. A. Sekhar and J. Mazumder, Defence Metallurgy Research Laboratory at Hyderabad, India, (Oxford & IBH Publishing, New Delhi, 1988) Vol. 1, p. 1.
61. S. H. HAN and R. TRIVEDI, *Acta Metall. Mater.* **42**(1) (1994) 25.
62. M. F. ASHBY, *Materials Science and Technology* **8**(2) (1992) 102.
63. E. SCHEIL and Z. METALLK, **34** (1942) 70.
64. J. A. BROOKS and K. W. MAHIN, *Solidification and structure of welds*, in "Welding: Theory and Practice," edited by D. L. Olson, R. Dixon and A. L. Liby (Elsevier Science, New York, 1990) p. 35.
65. M. C. FLEMINGS, "Solidification Processing" (McGraw-Hill, New York, 1974) p. 364.

Received 10 April 2000
and accepted 15 May 2001